PhotoniX

Universal orbital angular momentum spectrum analyzer for beams

Shiyao Fu[1,2] , Yanwang Zhai[1,2], Jianqiang Zhang[1,2], Xueting Liu[1,2], Rui Song[1,2], Heng Zhou[1,2] and Chunqing Gao[1,2]*

* Correspondence: gao@bit.edu.cn
[1]School of Optics and Photonics, Beijing Institute of Technology, Beijing 100081, China
[2]Key Laboratory of Photoelectronic Imaging Technology and System, Ministry of Education of the People's Republic of China, Beijing 100081, China

Abstract

The orbital angular momentum (OAM) of beams provides a new dimension, and have already found lots of applications in various domains. Among such applications, the precisely and quantitatively diagnostic of intensity distributions among different OAM modes, namely the OAM spectrum of a beam, is of great significance. In this paper we propose and experimentally validate a simple interferential method to achieve this goal. By analyzing the interference pattern formed by the beam and a reference field, the OAM spectrum can be obtained instantaneously. Furthermore, the proposed method is also available for more complex light fields, for instance, the multi-ring optical vortices. In the proof-of-concept experiment, the OAM spectra of both single-mode and *N*-fold multiplexed OAM modes with various intensity distributions are well detected. Our work offers a new way to precisely measure the OAM spectra of beams and will advance the development of many applications ranging from classical to quantum physics as the OAM based large-capacity data transmissions, rotation detection, quantum manipulation and so on.

Keywords: Orbital angular momentum, Orbital angular momentum spectrum, Laser field modulation, Interference

Introduction

Since Allen et al. proved in 1992 that a light beam whose complex amplitude comprises the helical term $\exp(il\phi)$ with l the topological charge and ϕ the azimuthal angle carries a definite amount of orbital angular momentum (OAM) [1], studies on beam's OAM came into researcher's sight and got great development. Previous studies have already illustrated that in such beams the OAM value carried by each photon equals to $l\hbar$, where $\hbar$ is Planck constant divided by 2π [1, 2]. Obviously the topological charge is the eigen value and determines the OAM value each photon carry. The OAM carried beams, usually referred to OAM beams, have doughnut intensity structures due to the center phase singularity [2]. The helical wavefront lead to a vortex-like intensity profile when interfering with fundamental Gaussian beams. Thus OAM beams also known as vortex beams [3] or twist beams [4]. These unique features of OAM beams make it possible to find wide applications in lots of domains ranging from classical to quantum physics, for instance, the large-capacity data

transmission [5–9], rotation probing [10–13], optical tweezers and micromanipulation [14, 15], imaging [16], quantum information [17, 18], gravitational wave detection [19, 20], astronomy [21] and so on.

It should be noticed that, multiple OAM states, not limited to single OAM mode, can be present simultaneously in one single beams. The intensity weights of different OAM channels in one single beam called OAM spectrum, which is similar with the well-known spectrum that denotes the intensity weights of various frequency or wavelength. Such OAM spectrum characterize the OAM beams, reflected on the intensity patterns and wavefront formset. That means the OAM spectrum have strong impacts on the performance for almost all the above application scenarios. Therefore the abilities to distinguish different OAM modes and diagnose the OAM spectrum are essential in an OAM-based optical system. Lots of schemes ranging from interferometry [22–26] to diffractometry [27–39] and then to integrated or meta-materials [39–43] have been proposed in the past few years to accomplish this goal, while they still have limitations in terms of the veracity, conciseness and universality. The early proposed approaches are mainly focusing on single OAM modes, appropriating for a beam that carries single OAM values, where the representative works contain interfering with plane wave [22, 23] and designing specific diffraction gratings [27–31]. Afterwards schemes to detect the multiplexed OAM states but exclude channel intensity proportions are demonstrated as composite fork-shaped gratings [32], Dammann vortex gratings [33, 34] and so on. Studies on the measurement of OAM spectrum started relatively late, where the main ideas fall into two categories. One is to effectively sort various OAM components, for instance, through the Mach-Zehnder interferometer [24–26] and the OAM mode sorter [35–38]. The other is the indirect measurement by other characteristic parameters, as gray-scale algorithm [44], rotational Doppler shift [45, 46], mode-matching method [47], spatial mode decomposition [48] et cetera. The exist approaches more or less face the problem of limited detection range, the measurement accuracy and so on. Moreover, almost none of the work covers the more common optical fields with complex intensity profiles like multi-ring vortices, Bessel-Gauss beams and so on.

In this paper, motivated by the wavefront diagnosing [49], we demonstrate a universal approach to accurately measure the OAM spectra of beams. In the proposed scheme, a stable but simple interferometer is built, where a probe Gaussian beam is introduced, and interfere with the beam to be measured. From the intensity profile of the measured beam, the probe Gaussian beam and the interference fields, the OAM spectrum can be well obtained with high accuracy. Additionally, the proposed scheme is universal and not limited to the common doughnut like OAM beams, implying that the OAM spectra of any beams including the multi-ring beams and more complex beams can be well analyzed. The results of the proof-of-concept experiments fit very well with prediction, showing good diagnostic performance. This work opens a new sight for the OAM spectrum analyzing for beams and will provide the basis of lots of advanced applications ranging from classical to quantum physics.

Methods

Realizing the universal OAM spectrum analyzer

To make the OAM spectrum analyzer universal for any beams, its principle must follow the basic definition of OAM spectrum. Note that here the discussion is confined

to scalar beams for simple, since any complex vector modes can be decomposed into two orthogonal scalar components [50, 51]. Thus the following discussions are also available for vector scenarios. The helical harmonic $\exp(il\phi)$ is the eigen wave function of OAM. Due to the azimuthally periodic distributions of helical harmonic, a beam $E(r, \phi,z)$ can be expanded directly under cylindrical coordinate through helical harmonics $\exp(il\phi)$ as [52, 53]:

$$E(r,\phi,z) = \frac{1}{\sqrt{2\pi}} \sum_{l=-\infty}^{+\infty} a_l(r,z) \exp(il\phi) \tag{1}$$

with the complex coefficient a_l:

$$a_l(r,z) = \frac{1}{\sqrt{2\pi}} \int_0^{2\pi} E(r,\phi,z) \exp(-il\phi)\mathrm{d}\phi \tag{2}$$

Thus the intensity of the l-th order helical harmonic is:

$$C_l = \int_0^{+\infty} |a_l(r,z)|^2 r\mathrm{d}r \tag{3}$$

Since the value C_l is independent of the parameter z, the relative intensity of such helical harmonic is:

$$R_l = \frac{C_l}{\sum_{q=-\infty}^{+\infty} C_q} \tag{4}$$

which is the OAM spectrum of $E(r,\phi,z)$. From Eqs. (2)–(4), obviously the OAM spectrum can be obtained once we know the complex amplitude $E(r,\phi,z)$, written as $E(r,\phi,z) = |E(r,\phi,z)|\exp[i\varphi(r,\phi,z)]$. The amplitude $|E|$ can be obtained directly by a CCD camera ($|E| = \sqrt{I}$, I is the captured intensity distributions). While the measurement of phase term ϕ is a little complex. Here a reference Gaussian beam E_R is employed to achieve this goal. After interfere with E_R, two various interfere patterns can be captured by introducing 0 and $\pi/2$ phase delay for E_R, as $I_{\cos} = |E + E_R|^2$ and $I_{\sin} = |E + E_R\exp(i\pi/2)|^2$. Then the phase Φ is calculated as $\Phi = \arctan[(I_{\sin}\text{-}I\text{-}I_R)/(I_{\cos}\text{-}I\text{-}I_R)]$, where I_R is the captured intensity profile of the reference Gaussian beam [49]. By now the complex amplitude of the beam to be analyzed is well recovered as:

$$E = \sqrt{I} \cdot \exp\left[i \arctan\left(\frac{I_{\sin} - I - I_R}{I_{\cos} - I - I_R}\right)\right] \tag{5}$$

Based on Eqs. (2)–(5), one can calculate the OAM spectrum conveniently through four measured intensity patterns I, I_R, $I_{\cos}$ and $I_{\sin}$, where the process is shown in Fig. 1. Furthermore, all the analyzing is done based on the basic definition, the helical harmonic decomposition of complex amplitude, rather than the intensity profiles, the singularity and so on. Thus the proposed approach is universal for any beams.

The setup

A proof-of-concept experimental setup is built to demonstrate the proposed OAM spectrum analyzer. As sketched in Fig. 2, a distributed feedback (DFB) laser with the wavelength 1.6 μm is employed as the source to produce fundamental Gaussian beams.
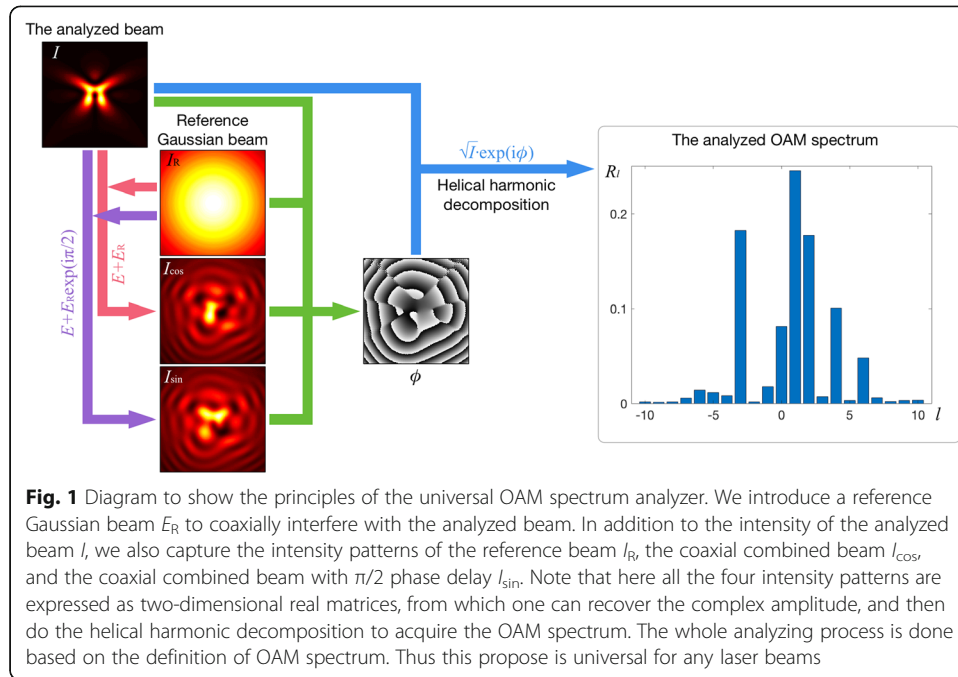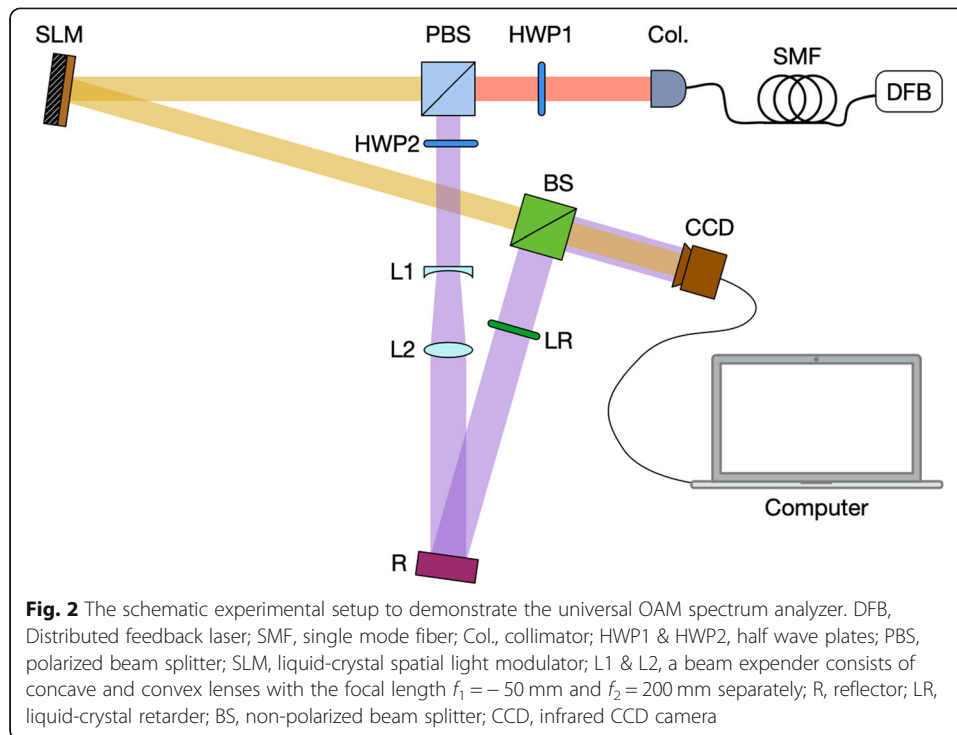
Fig. 1 Diagram to show the principles of the universal OAM spectrum analyzer. We introduce a reference Gaussian beam E_R to coaxially interfere with the analyzed beam. In addition to the intensity of the analyzed beam I, we also capture the intensity patterns of the reference beam I_R, the coaxial combined beam I_{cos}, and the coaxial combined beam with $\pi/2$ phase delay I_{sin}. Note that here all the four intensity patterns are expressed as two-dimensional real matrices, from which one can recover the complex amplitude, and then do the helical harmonic decomposition to acquire the OAM spectrum. The whole analyzing process is done based on the definition of OAM spectrum. Thus this propose is universal for any laser beams

After passing through a half wave plate (HWP) (HWP1 in Fig. 2), the Gaussian beams are incident into a polarized beam splitter (PBS) and thus divided into two parts, the p-polarizations and s-polarizations along the transmitted and reflected axes respectively. Their intensity proportion can be adjusted by rotating HWP1 properly. The transmitted p-polarized part is modulated by a liquid-crystal spatial light modulator (SLM) (Holoeye, PLUTO-TELCO-013-C) encoded with specially designed holograms and transformed into single-mode or N-fold multiplexed OAM beams. The reflected s-polarized part acts as reference beams. It propagates through a 45° arranged HWP (HWP2), a beam expander consists of a concave lens L1 ($f_1 = -50$ mm) and a convex lens L2 ($f_2 = 200$ mm), a reflector, and a liquid crystal retarder (LR) (Thorlabs, LCC1423-C), in sequence, and then combine with the OAM beams through a non-polarized beam splitter (BS). Here HWP2 is used to obtain p-polarized reference Gaussian beams, otherwise the reference beams won't interfere with the OAM beams. An infrared CCD camera (Xenics, Bobcat-320-star, resolution 320 × 256) is placed, with no specific positions, to record the two-dimensional intensity patterns I, I_R, I_{cos} and I_{sin}. Finally inputting such four patterns into the algorithm from Eqs. (2)–(5) to calculate the OAM spectrum.

Results and discussion

OAM spectrum analyzing for single modes

Firstly we employ the proposed OAM spectrum analyzer to measure single-mode OAM beams to see the analyzing performance. To generate single OAM beams, various holographic spiral phase plate (SPP) are encoded onto the SLM. When blocking reference Gaussian beam, one can obtain the intensity pattern of OAM beams I from CCD. Then blocking the tested OAM beam, one can obtain the intensity patterns of

Fig. 2 The schematic experimental setup to demonstrate the universal OAM spectrum analyzer. DFB, Distributed feedback laser; SMF, single mode fiber; Col., collimator; HWP1 & HWP2, half wave plates; PBS, polarized beam splitter; SLM, liquid-crystal spatial light modulator; L1 & L2, a beam expender consists of concave and convex lenses with the focal length $f_1 = -50$ mm and $f_2 = 200$ mm separately; R, reflector; LR, liquid-crystal retarder; BS, non-polarized beam splitter; CCD, infrared CCD camera

the reference Gaussian beam I_R. When neither of the two beams are blocked, we obtain I_{cos}. On this basis, applying a proper voltage to the LR to introduce a $\pi/2$ phase delay for reference beams to obtain I_{sin}. Once the four parameters I, I_R, I_{cos} and I_{sin}, namely four two-dimensional real matrices, are acquired, the OAM spectrum can be calculated through Eqs. (2)–(5). Fig. 3a displays the captured intensity patterns I, I_R, I_{cos} and I_{sin} of single OAM modes with the topological charges -3 and 8 respectively, and their corresponding simulated results. Obviously the experimental results match well with simulations. We analyze 21 various single-mode OAM beams with the topological charge range from -10 to 10, where the simulated and experimental OAM spectra are displayed separately in Fig. 3b and c. The heights of the bars in Fig. 3c are on the whole lower slightly than that of the simulated results in Fig. 3b, meanwhile some side undesired OAM modes are present especially for high-absolute-order single OAM beams.
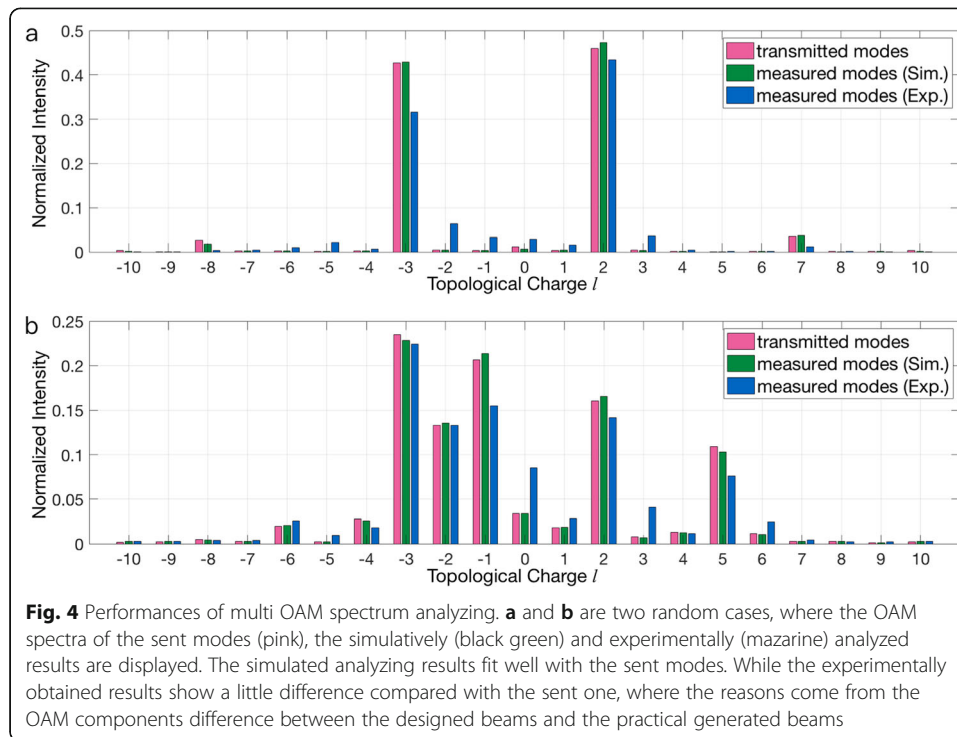
In the analyzed OAM spectra, the intensity of each single OAM channel is normalized to the total intensity, namely R_l in Eq. (4). Hence the value of vertical axis of desired OAM channel should be 1 and all else should be 0 ideally. However, the range of l is $-\infty \sim +\infty$ in Eq. (1), that is to say, there are infinite a_l expressed by Eq. (2), which is unavailable in the practical analyzing since such range must be bounded. One can imagine the selection of the l range must affect the measurement accuracy of the OAM spectrum. The larger the range, the more accurate the results. Here the range is chosen as $l \in [-20 \sim +20]$. For the simulated results shown in Fig. 3b, the root-mean-square errors (RMSE) of the analyzed OAM spectra for all the sent OAM channels are almost identical and fluctuates tinily around the mean value 3.62×10^{-6} (rounded off to three significant digits), which is small enough to prove the veracity and feasibility of

Fig. 3 Performances of single mode OAM spectrum analyzing. We use the CCD camera to record the intensity patterns of the OAM beam I, the reference Gaussian beam I_R, the interference field I_{cos} and the interference field with $\pi/2$ phase delay I_{sin}. Then OAM spectrum is calculated from the four patterns. **a** The simulatively and experimentally recorded intensity patterns I, I_R, I_{cos} and I_{sin} of single OAM modes with the topological charges $l = -3$ and $l = 8$. **b** displays the analyzed OAM spectra in simulation for various single OAM modes with topological charges $-10 \sim 10$, and **c** is the corresponding experimentally analyzed results

single OAM mode analyzing. As for the experimental results in Fig. 3c, the RMSE for each sent OAM channel is various and ranging from 3.39×10^{-5} to 3.06×10^{-2}, where the larger absolute value of topological charge corresponds to larger RMSE. The RMSE difference among different OAM channels results from that, OAM beams with larger absolute topological charge $|l|$ produced from a SLM with holographic SPP suffer more from the fixed pixel resolution of SLM than that with smaller absolute topological charge. The deep reason is the SLM's resolution cannot adapt the large phase jump in the center of high-absolute-order holographic SPP, leading to the lower mode purity and larger RMSE compared with that of the low-absolute-order OAM beams.

OAM spectrum analyzing for multiplexed modes

Next the proposed scheme is employed to analyze the N-fold multiplexed OAM beams. We compute some special designed holograms through Lin's algorithm [54] to generate multiplexed OAM beams with selective OAM spectra. Then analyzing their OAM spectra both simulatively and experimentally. As shown in Fig. 4, where the OAM
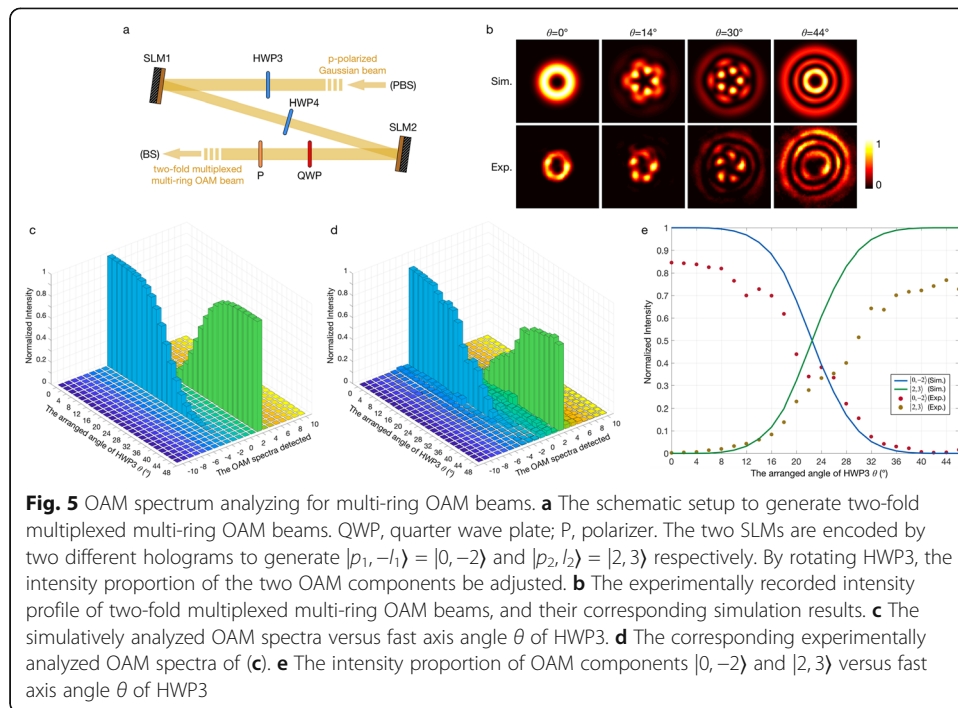
Fig. 4 Performances of multi OAM spectrum analyzing. **a** and **b** are two random cases, where the OAM spectra of the sent modes (pink), the simulatively (black green) and experimentally (mazarine) analyzed results are displayed. The simulated analyzing results fit well with the sent modes. While the experimentally obtained results show a little difference compared with the sent one, where the reasons come from the OAM components difference between the designed beams and the practical generated beams

spectra of the transmitted modes, the simulatively and experimentally obtained results are present. The RMSE is also evaluated, corresponding to simulation and experimental results separately are 2.87×10^{-3} and 2.00×10^{-2} for Fig. 4a, and 3.75×10^{-3} and 3.11×10^{-2} for Fig. 4b. From Fig. 4 the simulatively obtained OAM spectra fit very well with the sent one, implying the accuracy of the proposed scheme. However the experimentally analyzed OAM spectra demonstrate a little difference compared with the sent one, and the RMSE value is also increase. Such phenomena mainly result from that, the OAM components of the practical generated multiplex OAM beams are not exactly the distribution we expect. Spiral modes produced from phase-element (the SLM here) modulation will be affected by the phase discretization, and are prone to collapse [55]. Meanwhile the liquid crystal intermolecular forces within the SLM's screen will limit the electrically controlled rotation of liquid crystal molecules to some extent. Although such effects are small, they can still introduce non-complete phase modulation, and will be more serious for complex phase screen to generate multiplexed OAM beams. Usually for strict OAM components control, it is better to introduce feedback-assisted adaptive power-control to compensate OAM distributions [56]. Therefore the differences reflected by the mazarine bar in Fig. 4 are inevitable. Nevertheless the experimental OAM spectra are still very close to that of the sent one. The performance of the simulatively and experimentally analyzed OAM spectra proves the feasibility and availability of the proposed OAM spectrum analyzer.

OAM spectrum analyzing for complex fields
To further evaluate the universality of the proposed analyzer, the OAM spectrum for more complex fields as multiplexed multi-ring OAM beams are measured. The multi-

ring OAM beam have a multi-ring-shaped intensity profile with concentric circles, and meanwhile carries OAM due to its helical wavefront [1]. The multi-ring OAM beams reads $|p, l\rangle \propto L_p^{|l|}$ $(2r^2/\omega^2) \cdot \exp(il\phi)$, with p the radial index that determine the number of the concentric circles, ω the waist size, r the radial coordinate, and $L_p^{|l|}$ (ζ) the associated Laguerre polynomial. When $p = 0$, $L_0^{|l|}$ $(\zeta) = 1$, $|0, l\rangle \propto \exp(il\phi)$ represents the common single-ring single mode OAM beams. We measure the OAM spectrum of two-fold multiplexed multi-ring OAM beams with different radial indices to see the universal performance. Due to the complex concentric intensity distribution, it is hard to produce such beams through one single hologram. Here we cascade two SLM, each of which encodes a multi-ring SPP hologram [57] to generate one OAM component, thus to produce two-fold multiplexed multi-ring OAM beams. The SLM in Fig. 2 is replaced by the system given in Fig. 5a. The p-polarized Gaussian beam passes through an HWP (HWP3), and then incident in a SLM (SLM1). Due to the property of phase-only modulation of SLM [58], only the horizontal polarization part is modulated, and the output beam reads $\alpha |p_1, l_1\rangle|H\rangle + \beta|0, 0\rangle|V\rangle$, where $|H\rangle$ and $|V\rangle$ denotes the horizontally and vertically linear polarization bases respectively. α and β are intensity proportion which are determined by the angle θ of fast axis of HWP3, as $\alpha = \cos^2\theta$ and $\beta = \sin^2\theta$. HWP4 with 45° arranged fast axis is placed to exchange the two orthogonal linear polarizations, and obtain $\beta |0, 0\rangle|H\rangle + \alpha|p_1, l_1\rangle|V\rangle$. After modulated by another SLM (SLM2), we obtain $\beta |p_2, l_2\rangle|H\rangle + \alpha|p_1, -l_1\rangle|V\rangle$. Note that the $-l_1$ comes from the reflection of SLM2. Then the modulated beam pass through a 45° arrange quarter wave plate (QWP) and a horizontally placed polarizer (P) in sequence, and finally the two-fold multiplexed multi-ring OAM beams $(\alpha |p_1, -l_1\rangle + \beta|p_2, l_2\rangle)|H\rangle$ are generated. Additionally by rotating HWP3 one can arbitrary adjusting the intensity proportion between $|p_1, -l_1\rangle$ and $|p_2, l_2\rangle$.

Here we choose $|p_1, -l_1\rangle = |0, -2\rangle$ and $|p_2, l_2\rangle = |2, 3\rangle$ as example. With the rotation of HWP3 the measured OAM spectra will be changed accordingly. Fig. 5b lists some of the intensity patterns of experimentally captured multiplexed multi-ring OAM beams under various θ, which exhibit little difference compared with simulated patterns. Under different θ, we analyze both simulatively and experimentally obtained OAM spectra, as shown separately in Fig. 5c and d. In Fig. 5c, the envelope of OAM channels $|l=-2\rangle$ and $|l=3\rangle$ reflect the variation of intensity proportion α and β of the two components, and satisfy the sine square function as $\alpha = \cos^2\theta$ and $\beta = \sin^2\theta$, as displayed by the solid line in Fig. 5e, implying that the OAM spectra obtained through simulation meet well with theory. For the experimental results in Fig. 5d, except the desired OAM channels $|l=-2\rangle$ and $|l=3\rangle$, lots of adjacent OAM modes emerges, leading to the intensity decreasing of OAM channels $|l=-2\rangle$ and $|l=3\rangle$, compared with that of simulation. Such phenomenon is more apparent when separately showing the intensity variations of the two modes in Fig. 5e. The main reasons are the resolution limitation and the non-complete phase modulation of SLM as discussed previously. In addition, the intensity decrease of $|p_2, l_2\rangle = |2, 3\rangle$ is more serious than $|p_1, -l_1\rangle = |0, -2\rangle$, which result from that, $|p_2, l_2\rangle = |2, 3\rangle$ has three concentric circles and its generating hologram is more complex compared with that of single-ring $|p_1, -l_1\rangle = |0, -2\rangle$. Thus the non-complete phase modulation is also serious. Nevertheless, the curves formed by experimental analysis are also approximately sinusoidal squared, and have the same trend with the simulated results, which have already shown the performance of analyzing beams with complex intensity profile and proved the universality of the proposed analyzer.

Fig. 5 OAM spectrum analyzing for multi-ring OAM beams. **a** The schematic setup to generate two-fold multiplexed multi-ring OAM beams. QWP, quarter wave plate; P, polarizer. The two SLMs are encoded by two different holograms to generate $|p_1, -l_1\rangle = |0, -2\rangle$ and $|p_2, l_2\rangle = |2, 3\rangle$ respectively. By rotating HWP3, the intensity proportion of the two OAM components be adjusted. **b** The experimentally recorded intensity profile of two-fold multiplexed multi-ring OAM beams, and their corresponding simulation results. **c** The simulatively analyzed OAM spectra versus fast axis angle θ of HWP3. **d** The corresponding experimentally analyzed OAM spectra of (**c**). **e** The intensity proportion of OAM components $|0, -2\rangle$ and $|2, 3\rangle$ versus fast axis angle θ of HWP3

Additional discussions

There are some points to be emphasized. One of the key conditions of the OAM spectrum analysis here is the recovery of the beams' complex amplitude, which demands the coaxially interference of the beams and reference fields. If the beams to be measured interference tiltedly with reference beams, the phase term of the measured complex amplitude must comprise the tilted phase components, namely the fork-shaped phases. Since the helical harmonic decomposition is accomplished along azimuthal direction evenly, the presence of such tilted phase components will lead to the irrelevant measured OAM components. Therefore the tilt error surely decreases the accuracy of the OAM spectrum measurement.

The above experimental results have already shown favorable performance in analyzing coaxial multiplexed OAM modes. While the proposed scheme is unavailable for scenarios with de-centered multiplexed OAM states. Here the OAM spectrum is acquired from the helical harmonic decomposition of the recovered complex amplitude. Such decomposition needs a center, namely the origin of polar coordinate. If multiple de-centered OAM channels are present in one optical field, there must be multiple different center corresponding to various OAM components. However, the helical harmonic decomposition is done simultaneously for the field with all the present OAM channels, which means some of the OAM center must diverge from the decomposition center. Hence there must be measurement errors for OAM channels whose OAM center doesn't locate on the decomposition center.

In the practical measurement, the resolution of the employed CCD camera will also affect the accuracy of OAM spectrum diagnostic. Such phenomena can be vividly understood as such resolution determines the dispersion degree of the measured complex amplitude along azimuth. An additional simulation is done to show such influences, which can be seen in Supplementary Materials. Another concern is the

analyzing time, as how long does it take to analyze the OAM modes. Actually such time is the image processing time and mainly determined by the computer configuration. Here once the four intensity profiles are captured, the image processing needs about 1.953 s (under the condition of CPU: 2.9 GHz Intel Core i5, and graphics card: Intel Iris Graphics 6100 1536 MB). The whole system can surely be built more compact, where the main elements can be placed compactly in a slab, to meet with various application demands.

Conclusions

In summary, we have proposed a universal OAM spectrum analyzer for beams, where a reference Gaussian beam is introduced and combined coaxially with the initial beam, and then the OAM spectrum can be well calculated from the intensity patterns. The analyzing is based on one of the definitions of OAM spectrum, the helical harmonic decomposition, implying the proposed scheme is universal for arbitrary beams and not limited to doughnut-shaped OAM beams. Through the proposed approach, the analyzed OAM spectra fit very well with theory. The proof-of-concept experiments, as OAM spectrum analyzing for single mode OAM beams, multiplexed OAM beams, and beams with complex intensity distributions, are also carried out to demonstrate the practical performance of the OAM spectrum analyzer. The favorable results indicate well the universality, accuracy and practicability. This work opens a new sight for accurate OAM spectrum diagnostic and paves a way for the production of OAM comb [59] and other OAM based applications ranging from classical to quantum physics.

Supplementary information

Supplementary information accompanies this paper at https://doi.org/10.1186/s43074-020-00019-5.

Additional file 1.

References
1. Allen L, Beijersbergen MW, Spreeuw RJC, Woerdman JP. Orbital angular momentum of light and the transformation of Laguerre-Gaussian laser modes. Phys Rev A. 1992;45:8185–9.
2. Yao AM, Padgett MJ. Orbital angular momentum: origins, behavior and applications. Adv Opt Photonics. 2011;3: 161–204.

3.   Franke-Arnold S, Allen L, Padgett M. Advances in optical angular momentum. Laser Photon Rev. 2008;2:299–313.
4.   Molina-Terriza G, Torres JP, Torner L. Twisted photons. Nat Phys. 2007;3:305–10.
5.   Wang J, Yang JY, Fazal IM, Ahmed N, Yan Y, Huang H, Ren Y, Yue Y, Dolinar S, Tur M, Willner AE. Terabit free-space data transmission employing orbital angular momentum multiplexing. Nat Photonics. 2012;6:488–96.
6.   Bozinovic N, Yue Y, Ren Y, Tur M, Kristensen P, Huang H, Willner AE, Ramachandran S. Terabit- scale orbital angular momentum mode division multiplexing in fibers. Science. 2013;340:1545–8.
7.   Yu S. Potentials and challenges of using orbital angular momentum communications in optical interconnects. Opt Express. 2015;23:3075–87.
8.   Lei T, Zhang M, Li Y, Jia P, Liu GN, Xu X, Li Z, Min C, Lin J, Yu C, Niu H, Yuan X. Massive individual orbital angular momentum channels for multiplexing enabled by Dammann gratings. Light: Sci Appl. 2015;4:e257.
9.   Fu S, Zhai Y, Zhou H, Zhang J, Wang T, Yin C, Gao C. Demonstration of free-space one-to-many multicasting link from orbital angular momentum encoding. Opt Lett. 2019;44:4753–6.
10. Lavery MPJ, Speirits FC, Barnett SM, Padgett MJ. Detection of a spinning object using light's orbital angular momentum. Science. 2013;341:537–40.
11. Lavery MPJ, Barnett SM, Speirits FC, Padgett MJ. Observation of the rotational Doppler shift of a white-light, orbital-angular-momentum-carrying beam backscattered from a rotating body. Optica. 2014;1:1–4.
12. Fu S, Wang T, Zhang Z, Zhai Y, Gao C. Non-diffractive Bessel-gauss beams for the detection of rotating object free of obstructions. Opt Express. 2017;25:20098–108.
13. Zhai Y, Fu S, Yin C, Zhou H, Gao C. Detection of angular acceleration based on optical rotational Doppler effect. Opt Express. 2019;27:15518–27.
14. Grier DG. A revolution in optical manipulation. Nature. 2003;424:810–6.
15. Padgett M, Bowman R. Tweezers with a twist. Nat Photon. 2011;5:343–8.
16. Qiu X, Li F, Zhang W, Zhu Z, Chen L. Spiral phase contrast imaging in nonlinear optics: seeing phase objects using invisible illumination. Optica. 2018;5:208–12.
17. Fickler R, Lapkiewicz R, Plick WN, Krenn M, Schaeff C, Ramelow S, Zeilinger A. Quantum entanglement of high angular momenta. Science. 2012;338:640–3.
18. Larocque H, Gagnon-Bischoff J, Mortimer D, Zhang Y, Bouchard F, Upham J, Grillo V, Boyd RW, Karimi E. Generalized optical angular momentum sorter and its application to high-dimensional quantum cryptography. Opt Express. 2017;25: 19832–43.
19. Granata M, Buy C, Ward R, Barsuglia M. Higher-order Laguerre-gauss mode generation and interferometry for gravitational wave detectors. Phys Rev Lett. 2010;105:231102.
20. Noack A, Bogan C, Willke B. Higher-order Laguerre–gauss modes in (non-) planar four-mirror cavities for future gravitational wave detectors. Opt Lett. 2017;42:751–4.
21. Tamburini F, Thidé B, Molina-Terriza G, Anzolin G. Twisting of light around rotating black holes. Nat Phys. 2011;7:195–7.
22. Harris M, Hill C, Tapster P, Vaughan JM. Laser modes with helical wave-fronts. Phys Rev A. 1994;49:3119–22.
23. Soskin M, Gorshkov V, Vasnetsov M, Malos J, Heckenberg NR. Topological charge and angular momentum of light beams carrying optical vortices. Phys Rev A. 1997;56:4064–75.
24. Leach J, Padgett MJ, Barnett SM, Franke-Arnold S, Courtial J. Measuring the orbital angular momentum of a single photon. Phys Rev Lett. 2002;88:257901.
25. Lavery MPJ, Dudley A, Forbes A, Courtial J, Padgett MJ. Robust interferometer for the routing of light beams carrying orbital angular momentum. New J Phys. 2011;13:093014.
26. Zhang W, Qi Q, Zhou J, Chen L. Mimicking faraday rotation to sort the orbital angular momentum of light. Phys Rev Lett. 2014;112:153601.
27. Sztul HI, Alfano RR. Double-slit interference with Laguerre-Gaussian beams. Opt Lett. 2006;31:999–1001.
28. Hickmann JM, Fonseca EJS, Soares WC, Chavez-Cerda S. Unveiling a truncated optical lattice associated with a triangular aperture using light's orbital angular momentum. Phys Rev Lett. 2010;105:053904.
29. Zhang W, Wu Z, Wang J, Chen L. Experimental demonstration of twisted light's diffraction theory based on digital spiral imaging. Chin Opt Lett. 2016;14:110501.
30. Dai K, Gao C, Zhong L, Na Q, Wang Q. Measuring OAM states of light beams with gradually-changing-period gratings. Opt Lett. 2015;40:562–5.
31. Fu S, Wang T, Gao Y, Gao C. Diagnostics of the topological charge of optical vortex by a phase-diffractive element. Chin Opt Lett. 2016;14:080501.
32. Gibson G, Courtial J, Padgett M, Vasnetsov M, Pasko V, Barnett S, Franke-Arnold S. Free-space information transfer using light beams carrying orbital angular momentum. Opt Express. 2004;12:5448–56.
33. Zhang N, Yuan XC, Burge RE. Extending the detection range of optical vortices by Dammann vortex gratings. Opt Lett. 2010;35:3495–7.
34. Fu S, Wang T, Zhang S, Gao C. Integrating 5×5 Dammann gratings to detect orbital angular momentum states of beams with the range of −24 to +24. Appl Opt. 2016;55:1514–7.
35. Berkhout GCG, Lavery MPJ, Courtial J, Beijersbergen MW, Padgett MJ. Efficient sorting of orbital angular momentum states of light. Phys Rev Lett. 2010;105:153601.
36. Mirhosseini M, Malik M, Shi Z, Boyd RW. Efficient separation of the orbital angular momentum eigenstates of light. Nat Commun. 2013;4:2781.
37. Wen Y, Chremmos I, Chen Y, Zhu J, Zhang Y, Yu S. Spiral transformation for high-resolution and efficient sorting of optical vortex modes. Phys Rev Lett. 2018;120:193904.
38. Sahu R, Chaudhary S, Khare K, Bhattacharya M, Wanare H, Jha AK. Angular lens. Opt Express. 2018;26:8709–18.
39. Cicek K, Hu Z, Zhu J, Meriggi L, Li S, Nong Z, Gao S, Zhang N, Wang X, Cai X, Sorel M, Yu S. Integrated optical vortex beam receivers. Opt Express. 2016;24:28529–39.
40. Genevet P, Lin J, Kats MA, Capasso F. Holographic detection of the orbital angular momentum of light with plasmonic photodiodes. Nat Commun. 2012;3:1278.
41. Jin J, Luo J, Zhang X, Gao H, Li X, Pu M, Gao P, Zhao Z, Luo X. Generation and detection of orbital angular momentum via metasurface. Sci Rep. 2016;6:24286.

42. Devlin RC, Ambrosio A, Wintz D, Oscurato SL, Zhu AY, Khorasaninejad M, Oh J, Maddalena P, Capasso F. Spin-to-orbital angular momentum conversion in dielectric metasurfaces. Opt Express. 2017;25:377–93.

43. Chen P, Ma LL, Duan W, Chen J, Ge SJ, Zhu ZH, Tang MJ, Xu R, Gao W, Li T, Hu W, Lu YQ. Digitalizing self-assembled chiral superstructures for optical vortex processing. Adv Mater. 2018;30:1705865.

44. Fu S, Zhang S, Wang T, Gao C. Measurement of orbital angular momentum spectra of multiplexing optical vortices. Opt Express. 2016;24:6240–8.

45. Vasnetsov MV, Torres JP, Petrov DV, Torner L. Observation of the orbital angular momentum spectrum of a light beam. Opt Lett. 2003;28:2285–7.

46. Zhou HL, Fu DZ, Dong JJ, Zhang P, Chen DX, Cai XL, Li FL, Zhang XL. Orbital angular momentum complex spectrum analyzer for vortex light based on the rotational Doppler effect. Light Sci Appl. 2017;6:e16251.

47. Zhao P, Li S, Feng X, Cui K, Liu F, Zhang W, Huang Y. Measuring the complex orbital angular momentum spectrum of light with a mode-matching method. Opt Lett. 2017;42:1080–3.

48. D'Errico A, D'Amelio R, Piccirillo B, Cardano F, Marrucci L. Measuring the complex orbital angular momentum spectrum and spatial mode decomposition of structured light beams. Optica. 2017;4:1350–7.

49. Huang H, Ren Y, Yan Y, Ahmed N, Yue Y, Bozovich A, Erkmen BI, Birnbaum K, Dolinar S, Tur M, Willner AE. Phase-shift interference-based wavefront characterization for orbital angular momentum modes. Opt Lett. 2013;38:2348–50.

50. Zhan Q. Cylindrical vector beams: from mathematical concepts to applications. Adv Opt Photon. 2009;1:1–57.

51. Fu S, Gao C, Wang T, Zhai Y, Yin C. Anisotropic polarization modulation for the production of arbitrary Poincaré beams. J Opt Soc Am B. 2018;35:1–7.

52. Liu YD, Gao C, Gao M, Li F. Coherent-mode represen- tation and orbital angular momentum spectrum of partially coherent beam. Opt Commun. 2008;281:1968–75.

53. Schulze C, Dudley A, Flamm D, Duparr'e D, Forbes A. Measurement of the orbital angular momentum density of light by modal decomposition. New J Phys. 2013;15:073025.

54. Lin J, Yuan XC, Tao SH, Burge RE. Collinear superposition of multiple helical beams generated by a single azimuthally modulated phase-only element. Opt Lett. 2005;30:3266–8.

55. Qiao Z, Xie G, Wu Y, Yuan P, Ma J, Qian L, Fan D. Generating high-charge optical vortices directly from laser up to 288th order. Laser Photon Rev. 2018;12:1800019.

56. Li S, Wang J. Adaptive power-controllable orbital angular momentum (OAM) multicasting. Sci Rep. 2015;5:9677.

57. Ohtake Y, Ando T, Fukuchi N, Matsumoto N, Ito H, Hara T. Universal generation of higher-order multiringed Laguerre-Gaussian beams by using a spatial light modulator. Opt Lett. 2007;32:1411–3.

58. Moreno I, Davis JA, Hernandez TM, Cottrell DM, Sand D. Complete polarization control of light from a liquid crystal spatial light modulator. Opt Express. 2012;20:364–76.

59. Yang Y, Zhao Q, Liu L, Liu Y, Rosales-Guzmán C, Qiu CW. Manipulation of orbital-angular-momentum spectrum using pinhole plates. Phys Rev Appl. 2019;12:064007.

Publisher's Note